The Astrophysical Journal, 980:208 (8pp), 2025 February 20 https://doi.org/10.3847/1538-4357/adae0e


# Unraveling the Nature of HAWC J1844–034 with Fermi-LAT Data Analysis and Multiwavelength Modeling

Sovan Boxi[1], Saptarshi Ghosh[2], and Nayantara Gupta[1]
[1] Raman Research Institute, C. V. Raman Avenue, 5th Cross Road, Sadashivanagar, Bengaluru, Karnataka 560080, India; sovanboxi@rrimail.rri.res.in, nayan@rri.res.in
[2] Astroparticule et Cosmologie, Université Paris Cité, Paris 75013, France; ghosh@apc.in2p3.fr
*Received 2024 December 17; revised 2025 January 15; accepted 2025 January 20; published 2025 February 17*

## Abstract

The extended ultra-high-energy (UHE) gamma-ray source HAWC J1844–034 is closely associated with two other sources, HAWC J1843–032 and HWC J1846–025. Moreover, other gamma-ray observatories like HESS, LHAASO, and Tibet AS$_\gamma$ have detected UHE gamma-ray sources whose spatial positions coincide with the position of HAWC J1844–034. The UHE gamma-ray data from several observatories aid analysis of the spectral features of this source in detail at teraelectronvolt energies. Of the four pulsars near HAWC J1844–034, PSR J1844–0346 is closest to it and possibly supplies the cosmic-ray leptons to power this source. We have analyzed the Fermi–Large Area Telescope (LAT) data to explore this source's morphology and identify its spectral features in the Fermi-LAT energy band. After removing the contribution of the pulsar to the gamma-ray spectral energy distribution (SED) by pulsar-phased analysis, we obtained upper limits on the photon flux and identified the gigaelectronvolt counterpart PS J1844.2–0342 in the Fermi-LAT energy band with more than 5$\sigma$ significance, which may be a pulsar wind nebula (PWN). Finally, the multiwavelength SED is modeled, assuming HAWC J1844–034 is a PWN.

*Unified Astronomy Thesaurus concepts:* Pulsar wind nebulae (2215); Gamma-rays (637); High energy astrophysics (739)

## 1. Introduction

The ultra-high-energy (UHE) gamma-ray window has opened up a great opportunity to study the highest-energy cosmic accelerators in the Galaxy. The High-Altitude Water Cherenkov gamma-ray observatory (HAWC) detects gamma rays and cosmic rays of energies ranging from 100 GeV to beyond 100 TeV. The third HAWC catalog (A. Albert et al. 2020) of very-high-energy (VHE) gamma-ray sources has a list of 65 sources detected at more than 5$\sigma$ significance. The Large High Altitude Air Shower Observatory (LHAASO) released its first source catalog in 2024, which reports about 43 UHE gamma-ray sources (Z. Cao et al. 2024). Observations of teraelectronvolt gamma-ray sources by the High Energy Spectroscopic System (HESS) have revealed that most teraelectronvolt gamma-ray sources are spatially extended sources. Due to their association with supernova remnants (SNRs), molecular clouds, and pulsars, it is nontrivial to identify the origin of the extended emissions.

The HESS Galactic Plane Survey (HGPS) detected HESS J1843–033, a gamma-ray source with no clear association, emitting up to 30 TeV photons (HESS Collaboration et al. 2018). Subsequent observations by HAWC revealed two sources, 2HWC J1844–032 and eHWC J1842–035, near the HESS detection. These sources were associated with emissions extending up to 56 TeV (A. U. Abeysekara et al. 2021). The LHAASO experiment identified LHAASO J1843–0338, which emitted photons exceeding 100 TeV (Z. Cao et al. 2021), a potential counterpart of HESS J1843–033 and 2HWC J1844–032. M. Amenomori et al. (2022), using the Tibet AS$\gamma$ experiment, reported TASG J1844–038, a gamma-ray source located near HESS J1843–033. They detected emissions above 25 TeV with a significance of 6.2$\sigma$ and discussed two possible associations: the pulsar PSR J1844–0346 and the SNR G28.6–0.1. Earlier, D. J. Helfand et al. (1989) identified a radio complex near the region, including areas of nonthermal emission. Subsequent X-ray observations with Chandra and ASCA confirmed nonthermal radiation from high-energy electrons, consistent with a shell-type SNR (A. Bamba et al. 2001; M. Ueno et al. 2003). This suggested a possible hadronic origin for the gamma rays, supported by the source's extended diffuse structure and compatibility with the SNR's age. An alternative leptonic scenario involving a pulsar wind nebula (PWN) powered by PSR J1844–0346 has also been proposed. T. Sudoh et al. (2021) emphasized that the flat spectral index of TASG J1844–038 and the energetics of PSR J1844–0346 align with a teraelectronvolt PWN interpretation. They also qualitatively discussed an inverse-Compton-scattering scenario and its potential correlation with the extended VHE source.

The unidentified source HESS J1843–033 is modeled as a large extended Gaussian component resulting from the merging of two Gaussian components previously detected by the HGPS pipeline. The radio SNR G28.6–0.1 and the energetic pulsar PSR J1844–0346 are located within one of the previously detected Gaussian components. Figure 7 of J. Devin et al. (2021) shows the region's complexity and a peak significance at nearly 6$\sigma$ near the position of the synchrotron-emitting SNR G28.6–0.1. PSR J1844–0346 lies approximately 10′ from the center of SNR G28.6–0.1 (D. A. Zyuzin et al. 2018). J. Devin et al. (2021) investigated the region and found no evidence of radio or X-ray emissions indicative of a bright synchrotron PWN. They also argued that an association between this pulsar and SNR G28.6–0.1 is unlikely, even with the most optimistic distance estimates for G28.6–0.1. Given the characteristic age

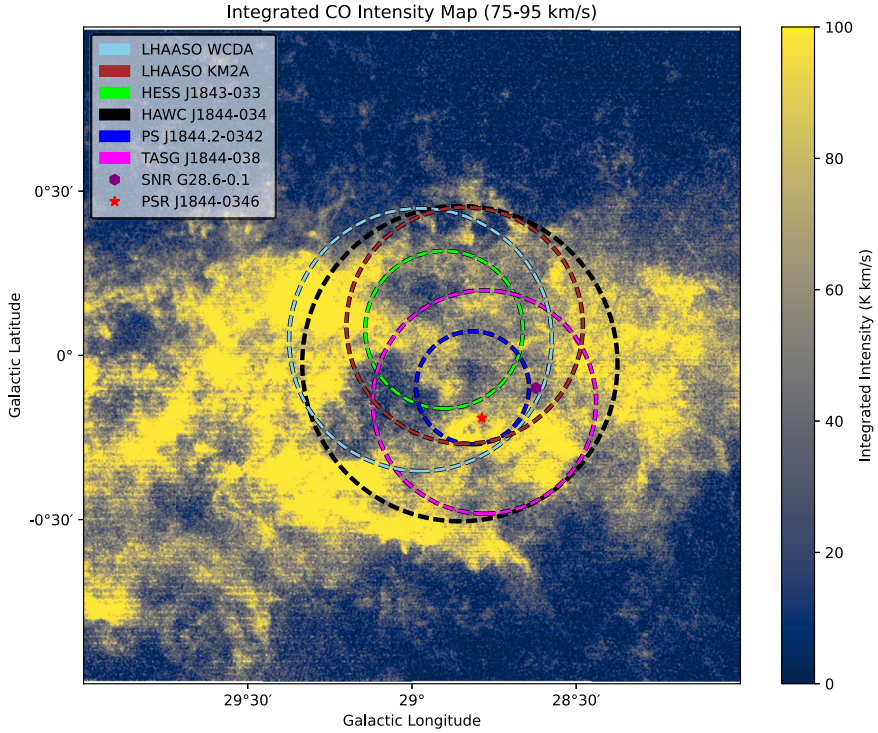


**Figure 1.** $2^\circ \times 2^\circ$ FUGIN survey molecular cloud distribution in the HAWC J1844−034 region of the integrated velocity channel from 75 to 95 km s$^{-1}$, investigated with $^{12}$CO($J = 1-0$) line emission using FUGIN public data (T. Umemoto et al. 2017). 1$\sigma$ extension contours from HESS (HESS Collaboration et al. 2018), HAWC (A. Albert et al. 2023), Fermi (this work), and TS-$\gamma$ (M. Amenomori et al. 2022) experiment counterparts are indicated in the left legend of the figure. LHAASO 39% extension radius measurements from LHAASO KM2A and WCDA are represented in brown and sky blue, respectively (Z. Cao et al. 2024). The positions of PSR J1844–0346 (R. N. Manchester et al. 2005) and SNR G28.6−0.1 (A. Bamba et al. 2001; M. Ueno et al. 2003) are marked in red and purple, respectively.

of PSR J1844−0346 and the decay of its magnetic field (S. J. Tanaka & F. Takahara 2010), synchrotron emission is expected to be faint and challenging to detect. However, MAGPIS radio and Spitzer infrared data revealed extended bright emission southeast of the pulsar, potentially linked to the star-forming region N49 (W. J. Dirienzo et al. 2012), embedded within the TASG extension (J. Devin et al. 2021; M. Amenomori et al. 2022).

Very recently, LHAASO detected the UHE gamma-ray source 1LHAASO J1843–0335u at an angular separation of $0.^\circ06$ (Z. Cao et al. 2024) from HESS J1843–033. It has been detected above 100 TeV with a test statistics (TS) value of 295.8 by the KM2A component of LHAASO.

A detailed observational data analysis of the source region of eHWC identified three components: HAWC J1844–034, HAWC J1843–032, and HAWC J1846–025 (A. Albert et al. 2023). The most significant and extended source among these three is HAWC J1844–034. We have analyzed the Fermi–Large Area Telescope (LAT) data from the source region to search for the emission from the extended source HAWC J1844–034. After pulsar-phased analysis of the Fermi-LAT data, we eliminated the gamma-ray emission from the pulsar and obtained upper limits from HAWC J1844–034. Finally, after combining the observational data from various observations, we have modeled the spectral energy distribution (SED), assuming the extended emission originates from the PWN powered by PSR J1844−0346.

## 2. HAWC J1844–034

HAWC J1844–034 is a bright extended gamma-ray source in the eHWC J1842–035 region, emitting photons at energies up to 175 TeV (A. Albert et al. 2023). The source exhibits an extended radially symmetric Gaussian morphology and has been detected with a $\sim 26\sigma$ significance. Its best-fit position is R.A.(J2000) $= 281.02^{+0.05}_{-0.05}$, decl.(J2000) $= -3.64^{+0.05}_{-0.004}$, with a 1$\sigma$ extension radius of $0.48^{+0.02}_{-0.02}$ (A. Albert et al. 2023).

Several VHE sources have been identified by different observatories in the HAWC region, as illustrated in Figure 1. For instance, the LHAASO detection of the UHE source LHAASO J1843–0338 has an angular separation of $0.^\circ27$ from the HAWC centroid with an extension of $0.^\circ3$. Tibet AS$\gamma$ experiments have observed another VHE source, TASG J1844–038, localized in that region with an offset of $0.^\circ14$ from the HAWC centroid and with an extension of $0.^\circ34$. The HESS HGPS survey found another interesting source, HESS J1843–033, near the HAWC center at an angular separation of $0.^\circ11$. Such spatial overlap of detections across multiple gamma-ray observatories highlights their excellent angular resolution at high energies (A. Albert et al. 2023). Despite these detections, the exact association for HAWC J1844–034 remains uncertain. Further investigation of this emission region's kinematical and morphological properties is required.

A possible association with the SNR G28.6−0.1 has been proposed. The shell-type SNR observed by A. Bamba et al. (2001) and M. Ueno et al. (2003) lies $0.^\circ28$ away from the HAWC J1844–034 centroid. It appears to interact with the molecular clouds in a velocity channel of 86 km s$^{-1}$, with an estimated distance of 9.6 ± 0.3 kpc (S. Ranasinghe & D. A. Leahy 2018). The molecular cloud distribution from the 75 to 95 km s$^{-1}$ channel investigated with the $^{12}$CO($J = 1-0$) emission line indicates the overlap of the TASG source with the SNR (Figure 1), suggesting that SNR G28.6−0.1 could be a possible PeVatron candidate (M. Amenomori et al. 2022).

However, modeling efforts from the HAWC collaboration suggest the estimated hadron spectrum has a smaller cutoff energy than the expected PeVatron cutoff energy (A. Albert et al. 2023). The gradient in the molecular cloud from our Figure 1 does not reflect the observed gamma-ray emission in the HAWC significance map (see Figure 1 of A. Albert et al. 2023), making the hadronic scenario more challenging.

There are at least three pulsars within the best-fit size of HAWC J1844–034: PSR J1843–0355 ($\dot{E} = 1.77 \times 10^{34}$ erg s$^{-1}$, $d \sim 5.8$ kpc), PSR J1844–0310 ($\dot{E} = 2.79 \times 10^{33}$ erg s$^{-1}$, $d \sim 6$ kpc), and PSR J1844–0346 ($\dot{E} = 4.2 \times 10^{36}$ erg s$^{-1}$, $d \sim 4.3/2.4$ kpc; R. N. Manchester et al. 2005; J. Wu et al. 2018; J. Devin et al. 2021). Also, PSR J1841–0345 ($\dot{E} = 2.7 \times 10^{35}$ erg s$^{-1}$, $d \sim 3.8$ kpc) is suggested as a possible counterpart source to LHAASO J1843–0338 in E. de Oña Wilhelmi et al. (2022), but it is located $0.^{\circ}63$ away from HAWC J1844−034, placing it outside of the extension of HAWC J1844−034. Therefore, we rule out PSR J1841−0345 from the counterpart source candidates. Among the remaining pulsars, PSR J1843−0355 and PSR J1844–0310 are both disfavored, due to their low spindown power, which is insufficient to account for the gamma-ray luminosity observed in HAWC J1844–034. Finally, PSR J1844–0346 has a spindown power approximately 2 orders of magnitude higher than the gamma-ray luminosity. This gigaelectronvolt pulsar was discovered in the Fermi-LAT blind search (C. J. Clark et al. 2017). The Fermi-LAT catalog identifies this as 4FGL J1844.4−0345 (S. Abdollahi et al. 2020). The exact distance of the pulsar is still unknown. The empirical estimates assuming gamma-ray luminosity scale with the spindown luminosity as $\sqrt{\dot{E}}$ (J. Wu et al. 2018), suggesting the distance to be 2.4 kpc (W. Zhang et al. 2024). Alternatively, the gamma-ray pulsar distance estimate based on the empirical formula (P. M. Saz Parkinson et al. 2010) suggests the pseudo-distance to be 4.3 kpc. Moreover, it is located closest to the best-fit positions of HAWC J1844–034, HESS J1843–033, and TASG J1844–038, with angular distances of $0.^{\circ}18$, $0.^{\circ}28$, and $0.^{\circ}05$, respectively.

Although leptonic and hadronic emission mechanisms associated with the SNR have been explored in the HAWC collaboration (A. Albert et al. 2023) modeling effort, several questions remain unanswered. X-ray data were not incorporated to constrain the magnetic field, and Fermi-LAT data were not included in the spectral fits. The authors qualitatively discussed the possibility of a PWN powered by PSR J1844–0346, but no direct modeling of the pulsar scenario was performed.

## 3. Fermi Data Analysis

### 3.1. Standard Analysis

We performed a detailed analysis of Fermi-LAT using 16 yr of data, from MET 239557417 (2008 August 4 15:43:36 UTC) to MET 739053099 (2024 June 2 20:31:34 UTC), in a region of interest (ROI) of $12^{\circ} \times 12^{\circ}$ centered on HAWC J1844–034. We referred to HAWC J1844–034 as the target source while pursuing our standard analysis. The Fermi-LAT point-spread function (PSF) improved significantly above 1 GeV, achieving an angular resolution of $0.^{\circ}1$ above 10 GeV. So, we restricted our analysis to 1–500 GeV, to leverage the better PSF at higher energies and to reduce the contamination from the flagged low-energy sources and molecular gas clumps.

The analysis used the latest comprehensive 4FGL-DR4 source catalog, along with the Galactic diffused template `gll_iem_v07.fits` and isotropic template `iso_P8R3_SOURCE_V3_v1.txt`. We have adopted the `P8R3_SOURCE_V3` instrument response function, with spatial binning of $0.^{\circ}05$ and eight energy bins per decade. Energy dispersion corrections were applied in all analyses except for the diffuse isotropic background. Photon events were categorized by their angular reconstruction quality into four PSF classes (PSF0, PSF1, PSF2, and PSF3), where PSF0 represents the worst quality and PSF3 the best. Likelihood analysis was performed for each PSF class separately, and the results were combined into a global likelihood function representing all the events in the ROI. We excluded the photons detected at zenith angles $< 90^{\circ}$ to minimize the contamination from the Earth-limb gamma rays caused by cosmic-ray interactions.

The `gta.optimize()` tool was executed two or three times, allowing the normalization parameters of the sources in the ROI to vary, to ensure convergence near the global likelihood maxima. The `gta.print_roi()` output identified weakly significant sources. We removed nondetected sources with TS $\leqslant 3$ or $N_{\rm pred} \leqslant 3$ to refine the model and improve the fit. The presence of numerous sources near the target source required a careful fitting approach. Nearby sources within $3^{\circ}$ were handled by freeing their normalization parameters within $3^{\circ}$ of the target while keeping other parameters fixed, to mitigate PSF-induced overlaps. High-TS sources and diffuse galactic and isotropic background normalizations were also freed, to ensure accurate modeling of the target source. Finally, we performed a fit using `gta.fit()` to fit all the parameters within the ROI, iterating until the fit quality reached 3. We used the `NEWMINUIT` optimizer for this purpose. The `NEWMINUIT` optimizer returned the best-fit model and flagged cases where convergence was problematic. The fit will give us the best possible model based on the input data. Diagnostic plots were inspected to confirm the fit quality. Then we employed the `gta.localize()` and `gta.find_sources()` algorithms to refine the unmodeled regions. We have discussed the relevant outputs in the results section.

### 3.2. Pulsar-phased Analysis

We analyzed 11 yr of Fermi-LAT data, collected between 2008 August and 2019 December, focusing on a $10^{\circ} \times 10^{\circ}$ ROI around the pulsar 4FGL J1844.4−0345. The analysis used Pass 8 data in the `Source` class (`evclass=128`) and `FRonT+BACK` type (`evtype=3`) events, covering the energy range from 100 MeV to 600 GeV. Event data files containing the `PULSE_PHASE` column were obtained directly from the Fermipy Pulsar catalog,[3] while the spacecraft file was downloaded from the Fermi-LAT data server. After having these files, we followed the analysis procedure given in the pulsar-phased analysis tutorial.[4] To limit contamination from the Earth-limb gamma-ray emission, events with a zenith angle greater than $105^{\circ}$ were excluded. We modeled the region using all point-like and extended sources listed in the 4FGL-DR4 catalog within a $12^{\circ} \times 12^{\circ}$ area, including galactic diffuse

[3] See the Fermi-LAT website at https://fermi.gsfc.nasa.gov/ssc/data/access/lat/3rd_PSR_catalog/3PC_HTML/J1844-0346.html.

[4] See the Fermipy documentation at https://fermipy.readthedocs.io/en/latest/notebooks/phase_analysis.html.

(gll_iem_v07.fits) and isotropic (iso_P8R3_SOURCE_V3_v1.txt) background templates. Following the Fermipy pulsar-phased analysis framework, we conducted a joint analysis of on-phase and off-phase data. First, we employed gta.optimize() to refine the fit parameters, by ensuring convergence to the global likelihood function. Subsequently, we performed the initial fit, allowing the Galactic diffused emission, isotropic background, and sources with TS $>$ 10 to vary. Diagnostic plots revealed positive residuals near the pulsar's position and negative residuals within 3° of the ROI. We freed the normalization parameters of the sources of the affected region, including the target source and background normalization, to improve the fit. A refit improved the ROI significantly, leaving no regions with TS $\sim 5\sigma$, except at the position of the pulsar (see Figure 2(b)). The TS value, which quantifies the source detection significance, is defined as:

$$\mathrm{TS} = 2(\ln \mathcal{L} - \ln \mathcal{L}_0), \quad (1)$$

where $\mathcal{L}$ represents the likelihood of source hypothesis (e.g., the presence of an additional source) and $\mathcal{L}_0$ the null hypothesis of the absence of a source. The significance of such detection can be estimated roughly as a square root of the TS value for one degree of freedom (J. R. Mattox et al. 1996). The model map of this fit shows some excess at the location of 4FGL J1844–0345. We investigated gta.find_sources with a $4\sigma$ threshold to identify additional sources contributing to the excess. We found few sources in the ROI, but we did find one specific source nearer to the pulsar than any 4FGL source, with an offset of $0.^{\circ}07$. Subsequently, once more, gta.fit() was done. Here, we have deleted the sources with TS $\leqslant 0$ or $N_{\mathrm{pred}} \leqslant 0$ from the model. The updated TS map, now including the new source, caused a significant reduction in the residuals at the pulsar position, which can be seen in Figure 2(b). Additionally, we present the on-phase TS map in Figure 2(a) for comparison. Finally, we evaluated the extension of the newly identified source using Fermipy's extension framework, the details of which are presented in the results section.

### 3.3. Analysis Results

For both analyses, we used a binned likelihood approach offered by ScienceTools version 2.2.0 and fermipy version 1.2.0 (M. Wood et al. 2017). The results from the standard likelihood analysis are discussed first, followed by the results of the pulsar-phased analysis. We performed localization, extension, and source-finding analysis across the entire energy range within the ROI to further refine the spatial and spectral modeling. The standard analysis revealed the closest source to our target was 4FGL J1844.4−0345, with an offset of $0.^{\circ}153$. This source exhibits steady, bright emission within the HAWC source extension, with a TS of 1173.37, and is a gigaelectronvolt pulsar, PSR J1844–0346 (C. J. Clark et al. 2017). Despite accounting for the pulsar, residual gamma-ray emission remained, which was not explained by the model. However, no additional point sources with $\sqrt{\mathrm{TS}} \sim 5$ were detected using Fermipy's source-finding algorithm. This outcome is expected, as such residuals would otherwise meet the source detection criterion and be included in the Fermi-LAT 4FGL catalog. We extracted the SED of 4FGL J1844.4–0345 using gta.sed(). The SED follows a power law with an exponential cutoff, with an explicit cutoff around 20 GeV. We repeated the analysis

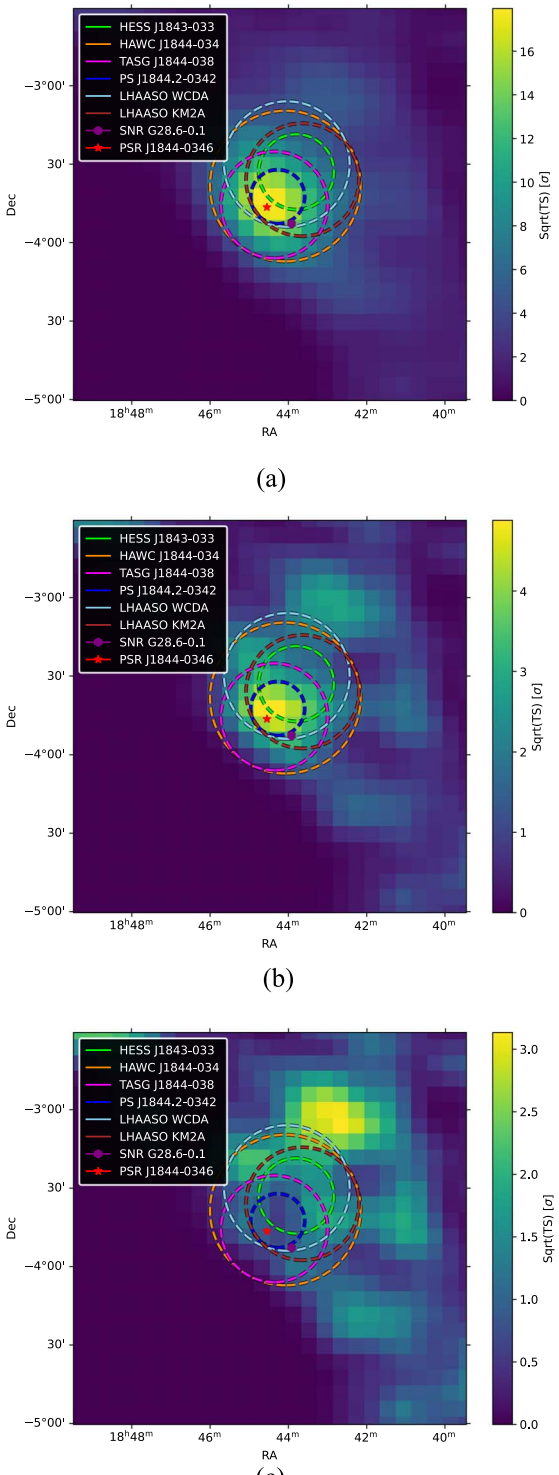


**Figure 2.** $\sqrt{\mathrm{TS}}$ maps from pulsar-phased analysis in the full energy range considered around the HAWC J1844–034 source. (a) The on-phase $\sqrt{\mathrm{TS}}$ map is shown. (b) The off-phase $\sqrt{\mathrm{TS}}$ map is shown, before looking for new sources through the gta.find_sources() tool. (c) The $5\sigma$ level reduction in the residuals at the position of the pulsar after modeling the new source PS J1844.2–0342. $1\sigma$ extension contours from the HESS (HESS Collaboration et al. 2018), HAWC (A. Albert et al. 2023), PS J1844.2–0342 (this work), and TS-$\gamma$ (M. Amenomori et al. 2022) experiment counterparts are indicated in the left legends of the figures. LHAASO 39% extension radius measurements from LHAASO KM2A and WCDA are represented in brown and sky blue, respectively (Z. Cao et al. 2024). The positions of PSR J1844–0346 (R. N. Manchester et al. 2005) and SNR G28.6−0.1 (A. Bamba et al. 2001; M. Ueno et al. 2003) are marked in red and purple, respectively.

using data above 20 GeV to explore the potential contribution beyond the pulsar. In this energy range, 4FGL J1844.4−0345 no longer exhibited any significant emission. Using the `gta.find_sources()`, we did not find any significant residual at the position of the pulsar beyond 20 GeV. We explored the pulsar-phased analysis during the off-pulse phase of the pulsar to investigate further.

The results from the pulsar-phased analysis are summarized here. We found few sources in the ROI with `gta.find_sources()`. According to the Fermipy convention, sources found by this method are added to the model and given designations PS JXXXX.X+XXXX, according to their position in celestial coordinates. In this case, only one specific source, named PS J1844.2−0342, resides within the HAWC extension and is nearer to the pulsar than any 4FGL source with an offset of $0.^{\circ}07$. The SED results are shown in Figure 3, separated into on-phase (pulsar-dominated) and off-phase (PWN-dominated) contributions. The on-phase SED is similar to the SED obtained from the standard analysis; both are fitted with a power law with an exponential cutoff. The cutoff $\sim$20 GeV is evident. The error bar represents the $1\sigma$ statistical error, and the confidence band represents the $1\sigma$ error obtained from the covariance matrix. Data points with $5\sigma$ or higher significance from the off-phase SED are retained for broadband SED modeling, while data points with lower significance were used to obtain upper limits with a 95% confidence level. The off-phase spectra exhibit a flat power-law profile. In contrast, the on-phase spectrum displays an exponential spectral cutoff, indicative of magnetospheric pulsar emission. We present the on-phase TS map in Figure 2(a). The residual in the northern part of Figure 2(c), after accounting for the new source, is outside the extension of our target HAWC source, J1844–034, and possibly due to HAWC J1843–032 (A. Albert et al. 2023, see their Figure 6), which we do not explicitly model.

We used `gta.extension()` and Fermipy-supported spatial templates to analyze this extended emission. The best-fit parameters, summarized in Table 1, favor a radially symmetric Gaussian model with an extension of $0.^{\circ}172$ and a TS extension value of 14.32, outperforming both radial disk and point-source models. We have also used the Akaike information criterion (AIC; H. Akaike 1974; K. Wu et al. 2022) to assess further the preferred model between the radial disk and radial Gaussian. The AIC is defined as $\mathrm{AIC} = 2k - 2\ln\mathcal{L}$, where $k$ is the number of free parameters in the model and $\mathcal{L}$ is the maximum likelihood obtained from the best fit. We found that the radial disk model has a slightly lower AIC compared to the radial Gaussian; however, the difference in AIC ($\Delta\mathrm{AIC} = 0.44$) is minimal and statistically insignificant, making it inconclusive to favor one model over the other based solely on this criterion. So, we relied on the $\mathrm{TS_{ext}}$ criterion to determine the best-fitting model. The extended source, named PS J1844.2−0342 (R.A. = 281.068, decl. = −3.708), likely corresponds to a PWN powered by the pulsar. It was detected with TS = 215.9 and fitted with a power-law spectrum and radially symmetric Gaussian profile. The best-fit power-law spectrum is expressed as $dN/dE = N_0(E/E_0)^{\gamma}$, where $N_0$ is the `prefactor`, $\gamma$ is the `spectral index`, and $E_0$ is the `energy scale`. The `prefactor` for the power-law spectrum is $4.011 \times 10^{-12} \pm 2.82 \times 10^{-13}\,\mathrm{MeV^{-1}\,cm^{-2}\,s^{-1}}$ with a `spectral index` of $\gamma = -2.256 \pm 0.04$ and energy scale $E_0$ of 1 GeV. The best-fit spectrum is shown in Figure 3(b). At an assumed distance of 2.4 kpc, the extension is 20 pc, corresponding to a physical size typical of a PWN. A zoomed-in $\mathrm{TS_{ext}}$ map highlighting the extended emission around the pulsar during the off phase is shown in Figure 4. We have summarized the key findings of our analysis in Table 2.

## 4. PWN SED Modeling with GAMERA

We assume that the PWN produces the emission observed by HAWC due to the radiative losses by the electrons and positrons being accelerated by its termination shock. The transport equation used to study the time evolution of the relativistic leptons is given by

$$\frac{\partial N(E,t)}{\partial t} = Q(E,t) - \frac{\partial[b(E,t)N(E,t)]}{\partial E} - \frac{N(E,t)}{t_{\mathrm{diff}}}, \quad (2)$$

where $N(E, t)$ is the resulting particle spectrum at any time $t$. $t_{\mathrm{diff}}$ is the escape time of high-energy leptons leaving the nebula via Kolmogorov diffusion. $b = b(E, t)$ includes synchrotron and inverse-Compton energy losses of the relativistic leptons. $Q(E, t)$ is the injection spectrum.

We employed the one-zone PWN model, including the energy-dependent modeling of the pulsar energy output, ambient magnetic field, and time-dependent injection, following closely the HESS collaboration paper (F. Aharonian et al. 2023). We modeled the time evolution of the particle distribution and radiation SED using GAMERA (J. Hahn et al. 2022). The parameters of the model are of two types: fixed input parameters, whose values come from observations, and adjusted parameters, whose values have been adjusted to fit the SED. The particle injection spectrum followed the power-law index with an exponential cutoff. The cutoff energy is treated as a free parameter, and it is denoted as $E_c$. The time evolutions of the pulsar period, pulsar spindown power, and magnetic field have been used from B. M. Gaensler & P. O. Slane (2006) and C. Venter & O. C. de Jager (2007). The normalization of the injected particle spectrum is determined by $\epsilon \times \dot{E}(t)$, where $\epsilon$ is the $e^+e^-$ power fraction. The evolution of the spindown luminosity is given by

$$\dot{E}(t) = \dot{E}_0\left(1 + \frac{t}{\tau_0}\right)^{-2}. \quad (3)$$

The time-varying PWN magnetic field is given by

$$B(t) = B_0\left[1 + \left(\frac{t}{\tau_0}\right)^{0.5}\right]^{-1}, \quad (4)$$

where the spindown timescale is given by

$$\tau_0 = \frac{P_0^2 P^{-1}}{2\dot{P}}. \quad (5)$$

The characteristic age of the pulsar is given by $\tau_c = P/2\dot{P}$, where $P_0$ and $\dot{P}_0$ are the pulsar birth period and corresponding period derivative, respectively. $P$ and $\dot{P}$ mean the current-day pulsar period and its derivative. These two parameter values are known from the pulsar catalog (R. N. Manchester et al. 2005). We have assumed a birth period of the pulsar as 85 ms, shown in Table 3, which gives a value of $\tau_0 = 6.5$ kyr. We adopted the canonical braking index of the pulsar $n = 3$. Similar assumptions regarding the birth period and braking index have been made in several studies, such as K. Wu et al. (2022) and

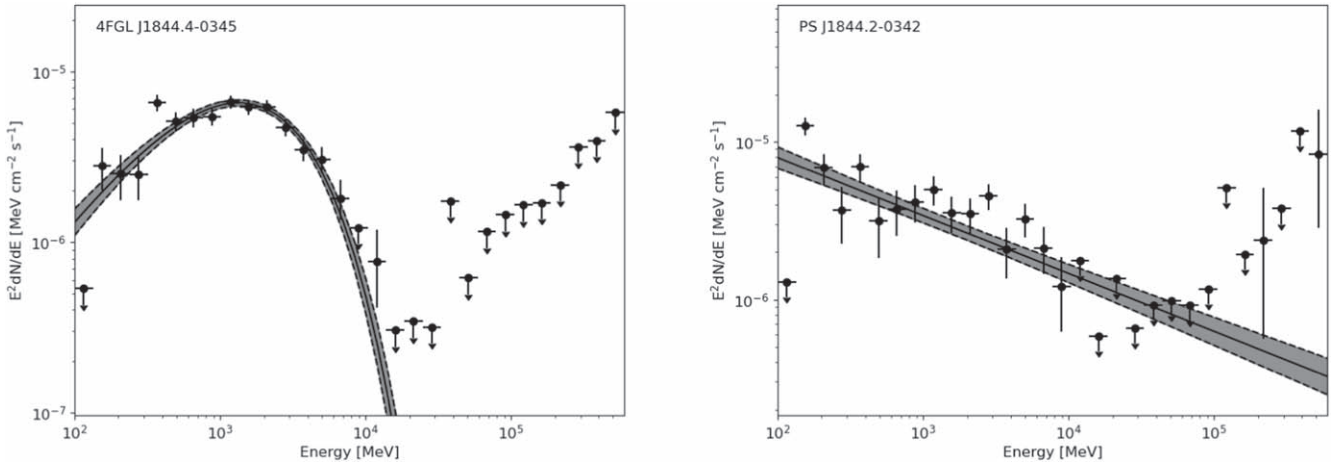


**Figure 3.** SEDs obtained from phased analysis of the PSR J1844-0346: (a) on phase; (b) off phase.

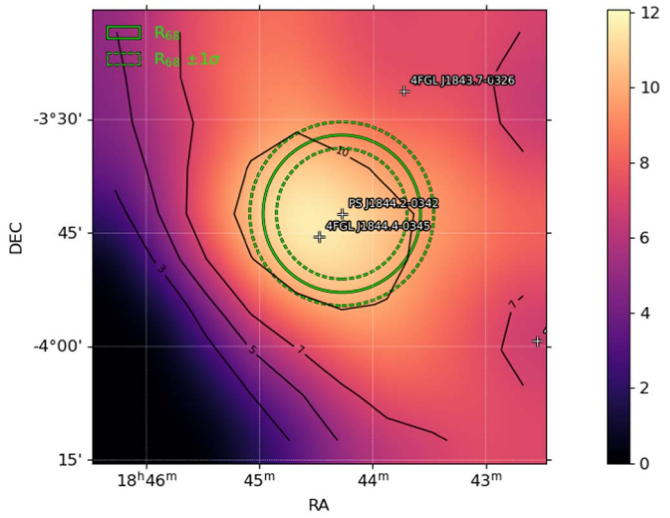


**Figure 4.** Zoomed-in $TS_{ext}$ map in full energy range highlighting the extended emission around the pulsar during the off phase. The $1\sigma$ extension of the newly identified source, PS J1844.2–0342, is marked in the figure.

**Table 1**
Source Properties

| Spatial Template | Best-fit Extension (deg) | $TS_{ext}$ Significance |
|---|---|---|
| Radial Gaussian | 0.172 | 14.32 |
| Radial Disk | 0.173 | 13.73 |

F. Aharonian et al. (2023). The more general form of the above formulas can be found in B. M. Gaensler & P. O. Slane (2006). The true age has to be close to 5 kyr, which is the difference between $\tau_c = 11.6$ kyr and $\tau_0 = 6.5$ kyr, following the general relation given in Equation (6):

$$\tau_0 = \frac{P_0}{(n-1)\dot{P}_0} = \frac{2\tau_c}{(n-1)} - t_{\rm age}. \quad (6)$$

We have computed the radiative cooling losses of the ultrarelativistic electrons due to inverse-Compton, synchrotron, and nonradiative loss due to diffusive escape. In the GAMERA framework, the complete Klein–Nishina cross section for inverse-Compton scattering (G. R. Blumenthal & R. J. Gould 1970) is utilized to compute the photon flux resulting from the relativistic electrons. For calculating the inverse-Compton emission from the interstellar radiation field target photon field, we have used the stellar and dust contribution in the position of the source, as given in C. C. Popescu et al. (2017). We have included the energy-dependent diffusion loss of cosmic-ray electrons using the following form of diffusion coefficient:

$$D = D_0\left(\frac{E}{E_0}\right)^{\delta}, \quad (7)$$

where $D_o = 1.1 \times 10^{28}\,{\rm cm^2\,s^{-1}}$ is the diffusion coefficient normalized at $E_0 = 40$ TeV and $\delta = 0.33$ (Kolmogorov scaling). This delta parameter has a very weak dependence on the observed data. These values are similar to those used for other pulsar halos (A. U. Abeysekara et al. 2017). The values of the parameters used to fit the observational data are presented in Table 3, and the SED modeling is shown in Figure 5. Most of the gamma-ray data points are fitted with the simulated SED obtained from our model, though we do not have any data points at X-ray or lower frequencies to constrain our model. It is well discussed in earlier studies that the model parameters cannot be constrained well with the limited number of data points (F. Aharonian et al. 2023). We do not have any data points in the radio, optical, or X-ray frequencies. In the VHE regime, we have around 13 data points; we tried to fit them by adjusting the values of six parameters. Given some of the model parameters are correlated and not always well constrained from the available data, the derived values of the parameters should not be considered as definitive values. Instead, they represent a plausible combination that provides a reasonable description of the observed data.

## 5. Discussion and Conclusion

The UHE gamma-ray source HAWC J1844–034 is closely associated with several other sources, HAWC J1843–032 and HWC J1846–025. In addition, LHAASO J1843–0338, TASG J1844–038, and HESS J1843–033 are the possible counterparts

**Table 2**
Summary of Analysis Findings

| Analysis Type | Key Findings |
|---|---|
| Standard Analysis | (1) The closest identified source was 4FGL J1844.4−0345, a gigaelectronvolt pulsar with a TS value of 1173.37 and an angular offset of $0.^{\circ}153$.<br>(2) The SED of 4FGL J1844.4−0345 follows a power law with an exponential cutoff, with the cutoff at ∼20 GeV. |
| Pulsar-phased Analysis | (1) In the off phase of the pulsar, a new source, PS J1844.2−0342, was identified at an offset of $0.^{\circ}07$ from the pulsar, located within the HAWC source extension, with a high-TS value of 216.<br>(2) The new source has an extension of $0.^{\circ}172$ with extended hypothesis $TS_{ext}$ significance greater than $3\sigma$.<br>(3) The off-pulse emission suggests contributions from extended sources, potentially a PWN. |

**Table 3**
Pulsar and Model Parameters

| Parameter | Description | Value | Units |
|---|---|---|---|
| | *Input Parameters* | | |
| $d$ | Pulsar distance[a] | 2.4 | kpc |
| $\dot{E}$ | Pulsar spindown power[b] | $4.2 \times 10^{36}$ | erg $s^{-1}$ |
| $\tau_c$ | Pulsar characteristic age[b] | 11.6 | kyr |
| $P$ | Pulsar period[b] | 113 | ms |
| $\dot{P}$ | Pulsar period derivative[b] | $1.55 \times 10^{-13}$ | s $s^{-1}$ |
| $n$ | Pulsar braking index[c] | 3 | ⋯ |
| $E_{\rm min}$ | Min energy of $e^+e^-$ | 1.0 | GeV |
| $E_{\rm max}$ | Max energy of $e^+e^-$ | 300 | TeV |
| | *Adjusted Parameters* | | |
| $\epsilon$ | $e^+e^-$ power fraction | 0.45 | ⋯ |
| $B$ | Magnetic field | 3.4 | $\mu$G |
| $P_0$ | Pulsar birth period | 85 | ms |
| $E_c$ | Cutoff energy | 175 | TeV |
| $\alpha$ | Injection spectrum index | 1.8 | ⋯ |
| $t_{\rm age}$ | Age of pulsar | 4.7 | kyr |

**Notes.** Input parameters are taken from observational measurements and theoretical models. Adjusted parameters are fit to the model.
[a] J. Wu et al. (2018).
[b] R. N. Manchester et al. (2005).
[c] M. Amenomori et al. (2022).

detected by LHAASO, Tibet $AS_\gamma$, and HESS, respectively. We have analyzed the Fermi-LAT data in the region of the HAWC source to find the emission from the extended source. The results of our data analysis are summarized in Table 2. The off-pulse emission suggests the possibility of the existence of a PWN that could be responsible for the UHE gamma-ray emission. In the Fermi-LAT energy band, we have obtained upper limits on the gamma-ray flux that are used to constrain the model parameters while modeling the multiwavelength SED in Figure 5. The values of the parameters of the pulsar PSR J1844–0346 are constrained from observations. They are denoted as input parameters in Table 3. The values of the other parameters, including the pulsar birth period, are adjusted to fit the observational data. Our model is consistent with the observational data.

W. Zhang et al. (2024) studied the possibility of teraelectronvolt gamma-ray emission from the putative PWNs associated with four pulsars. One of these pulsars is PSR J1844–0346. They showed that the teraelectronvolt emissions of the potential PWNs of the pulsars PSR 1838–0537 and PSR J1844–0346 are relatively high compared to those associated with PSR J1208–6238 and PSR J1341–6220. Their results suggested that this teraelectronvolt emission could be detectable by S-CTA and even by HESS for long-duration observations. The X-ray observations from the PWNs would be useful to constrain the models.

M. Araya & J. A. Álvarez-Quesada (2024) analyzed almost 15 yr of data recorded by Fermi-LAT in the region of the teraelectronvolt gamma-ray source 1LHAASO J1945+2424. The teraelectronvolt source is more extended than the Fermi-LAT source and the gigaelectronvolt spectrum connects smoothly with the teraelectronvolt spectrum. A $4\sigma$ excess was found in their TS map at the location of the source 4FGL J1948.8+2420 as well as at other nearby locations within the extension of the source 1LHAASO J1945+2424. They searched for new sources within their ROI. They found 10 new sources, three of which—PS J1945.2+2419, PS J1945.3+2449, and PS J1948.7+2422—are located within the 39% containment region of the WCDA-detected source. They replaced the three newly found sources with an extended source modeled by a 2D Gaussian. They used the flux upper limits and data points from this extended source in the Fermi-LAT energy band to model the multiwavelength SED of 1LHAASO J1945+2424 assuming both SNR and PWN scenarios.

In this work, we have identified a new source, PS J1844.2−0342, near the pulsar PSR J1844–0346; the details are given in Table 2, and further observations are necessary for the confirmation of our result. In Figure 2(c), it is shown that SNR G28.6–0.1 is outside the $1\sigma$ extension region of PS J1844.2−0342, hence we suggest that PS J1844.2−0342 is likely to be the PWN of PSR J1844–0346.

Recently, in many papers, the Fermi-LAT data have been analyzed to investigate the emission from extended teraelectronvolt halos (M. Di Mauro et al. 2021; J. Li et al. 2021; S. Abe et al. 2023; X. Guo & Y. Xin 2024; Y. Xiao et al. 2024). Fermi-LAT data analysis is very useful in exploring the gigaelectronvolt counterparts of the teraelectronvolt sources and subsequently identifying their origin. If both an SNR and pulsar are present within the teraelectronvolt halo, in some cases with the spatial position and morphology of the extended emission in the Fermi-LAT energy band, it would be possible to identify whether the SNR or the pulsar is the more likely counterpart of the teraelectronvolt halo.

We conclude from our results that the extended gigaelectronvolt source PS J1844.2−0342 may be the PWN of pulsar PSR J1844–0346, and it is the gigaelectronvolt counterpart of the teraelectronvolt extended source HAWC J1844–034. We have modeled HAWC J1844–034 assuming a PWN origin of teraelectronvolt emission. More observational data at lower frequencies would be helpful to unravel the nature of HAWC J1844–034.

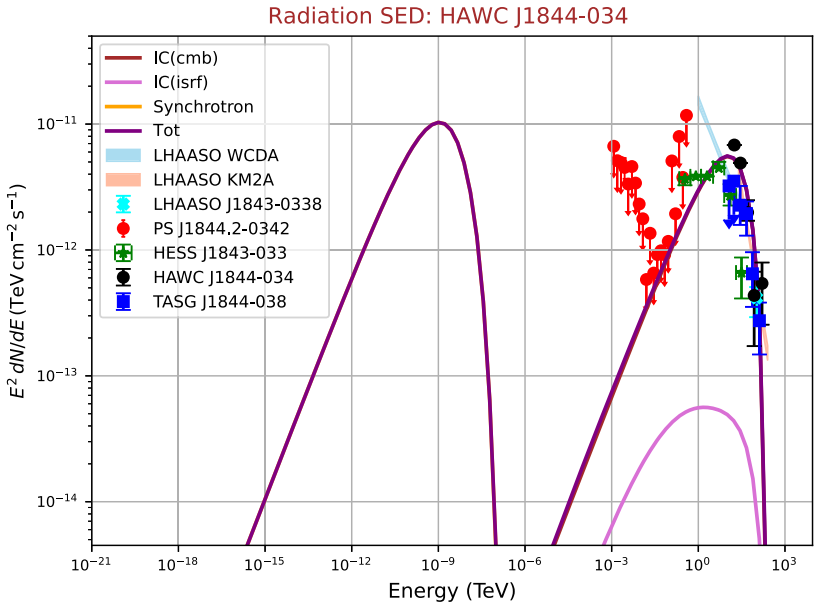


**Figure 5.** Gamma-ray data from HAWC (A. Albert et al. 2023), LHAASO (Z. Cao et al. 2021, 2024), Tibet (T. Sudoh et al. 2021), and HESS (HESS Collaboration et al. 2018) shown with Fermi-LAT upper limits obtained from our analysis. The SED obtained from our modeling is shown with a solid line.


## Acknowledgments

The authors thank the referee for helpful comments.



## ORCID iDs

Sovan Boxi https://orcid.org/0009-0004-1305-9578
Saptarshi Ghosh https://orcid.org/0000-0001-8585-9743
Nayantara Gupta https://orcid.org/0000-0002-1188-7503


## References


Abdollahi, S., Acero, F., Ackermann, M., et al. 2020, ApJS, 247, 33
Abe, S., Aguasca-Cabot, A., Agudo, I., et al. 2023, A&A, 673, A75
Abeysekara, A. U., Albert, A., Alfaro, R., et al. 2017, Sci, 358, 911
Abeysekara, A. U., Albert, A., Alfaro, R. J., et al. 2021, ICRC (Berlin), 37, 828
Aharonian, F., Ait Benkhali, F., Aschersleben, J., et al. 2023, A&A, 672, A103
Akaike, H. 1974, ITAC, 19, 716
Albert, A., Alfaro, R., Alvarez, C., et al. 2020, ApJ, 905, 76
Albert, A., Alvarez, C., Rojas, D. A., et al. 2023, ApJ, 954, 205
Amenomori, M., Asano, S., Bao, Y. W., et al. 2022, ApJ, 932, 120
Araya, M., & Álvarez-Quesada, J. A. 2024, MNRAS, 527, 8006
Bamba, A., Ueno, M., Koyama, K., & Yamauchi, S. 2001, PASJ, 53, L21
Blumenthal, G. R., & Gould, R. J. 1970, RvMP, 42, 237
Cao, Z., Aharonian, F., An, Q., et al. 2024, ApJS, 271, 25
Cao, Z., Aharonian, F. A., An, Q., et al. 2021, Natur, 594, 33
Clark, C. J., Wu, J., Pletsch, H. J., et al. 2017, ApJ, 834, 106
de Oña Wilhelmi, E., López-Coto, R., Amato, E., & Aharonian, F. 2022, ApJL, 930, L2
Devin, J., Renaud, M., Lemoine-Goumard, M., & Vasileiadis, G. 2021, A&A, 647, A68
Di Mauro, M., Manconi, S., Negro, M., & Donato, F. 2021, PhRvD, 104, 103002
Dirienzo, W. J., Indebetouw, R., Brogan, C., et al. 2012, AJ, 144, 173
Gaensler, B. M., & Slane, P. O. 2006, ARA&A, 44, 17
Guo, X., & Xin, Y. 2024, ApJ, 965, 28
Hahn, J., Romoli, C., & Breuhaus, M., 2022 GAMERA: Source Modeling in Gamma Astronomy, Astrophysics Source Code Library, ascl:2203.007
Helfand, D. J., Velusamy, T., Becker, R. H., & Lockman, F. J. 1989, ApJ, 341, 151
HESS Collaboration, Abdalla, H., Abramowski, A., et al. 2018, A&A, 612, A1
Li, J., Liu, R.-Y., de Oña Wilhelmi, E., et al. 2021, ApJL, 913, L33
Manchester, R. N., Hobbs, G. B., Teoh, A., & Hobbs, M. 2005, AJ, 129, 1993
Mattox, J. R., Bertsch, D. L., Chiang, J., et al. 1996, ApJ, 461, 396
Popescu, C. C., Yang, R., Tuffs, R. J., et al. 2017, MNRAS, 470, 2539
Ranasinghe, S., & Leahy, D. A. 2018, MNRAS, 477, 2243
Saz Parkinson, P. M., Dormody, M., Ziegler, M., et al. 2010, ApJ, 725, 571
Sudoh, T., Linden, T., & Hooper, D. 2021, JCAP, 2021, 010
Tanaka, S. J., & Takahara, F. 2010, ApJ, 715, 1248
Ueno, M., Bamba, A., Koyama, K., & Ebisawa, K. 2003, ApJ, 588, 338
Umemoto, T., Minamidani, T., Kuno, N., et al. 2017, PASJ, 69, 78
Venter, C., & de Jager, O. C. 2007, in Proc. 363 WE-Heraeus Seminar on Neutron Stars and Pulsars 40 years after the Discovery, ed. W. Becker & H. H. Huang (Garching bei München: Max Planck Institut für extraterrestrische Physik), 40
Wood, M., Caputo, R., Charles, E., et al. 2017, ICRC (Busan), 301, 824
Wu, J., Clark, C. J., Pletsch, H. J., et al. 2018, ApJ, 854, 99
Wu, K., Zhou, L., Gong, Y., & Fang, J. 2022, MNRAS, 519, 1881
Xiao, Y., Wu, K., & Fang, J. 2024, ApJ, 972, 84
Zhang, W., Torres, D. F., García, C. R., Li, J., & Mestre, E. 2024, A&A, 691, A332
Zyuzin, D. A., Karpova, A. V., & Shibanov, Y. A. 2018, MNRAS, 476, 2177